

Synthesis and characterization of lithium-conducting composite polymer-ceramic membranes for use in nonaqueous redox flow batteries

Yasser Ashraf Gandomi,^{a, ‡} Irina V. Krasnikova,^{b, ‡} Nikita O. Akhmetov,^b Nikolay A. Ovsyannikov,^b Mariam A. Pogosova,^b Nicholas J. Matteucci,^a Christopher T. Mallia,^c Bertrand J. Neyhouse,^a Alexis M. Fenton Jr.,^a Fikile R. Brushett,^{a,} and Keith J. Stevenson,^{b,*}*

^aDepartment of Chemical Engineering, Massachusetts Institute of Technology, Cambridge, MA
02139, USA

^bCenter for Electrochemical Energy Storage, Skolkovo Institute of Science and Technology,
Moscow, Russian Federation

^cDepartment of Materials Science and Engineering, Massachusetts Institute of Technology,
Cambridge, MA 02139, USA

‡ These authors contributed equally

** Corresponding authors*

Abstract

Redox flow batteries (RFBs) are a burgeoning electrochemical platform for long-duration energy storage, but present embodiments are too expensive for broad adoption. Nonaqueous redox flow batteries (NAqRFBs) seek to reduce system costs by leveraging the large electrochemical stability window of organic solvents (> 3 V) to operate at high cell voltages and to facilitate the use of redox couples that are incompatible with aqueous electrolytes. However, a key challenge for emerging nonaqueous chemistries is the lack of membranes/separators with suitable combinations of selectivity, conductivity, and stability. Single-ion conducting ceramics, integrated with polymeric fillers to make flexible composites, may offer a pathway to the performance attributes needed for competitive nonaqueous systems. Here, we explore composite polymer-inorganic binder-filler membranes for lithium-based NAqRFBs, investigating two different ceramic compounds with NASICON-type (NASICON: sodium (Na) Super Ionic CONductor) crystal structure, $\text{Li}_{1.3}\text{Al}_{0.3}\text{Ti}_{1.7}(\text{PO}_4)_3$ (LATP) and $\text{Li}_{1.4}\text{Al}_{0.4}\text{Ge}_{0.2}\text{Ti}_{1.4}(\text{PO}_4)_3$ (LAGTP), blended with a polyvinylidene fluoride (PVDF) polymeric matrix. We characterize the physicochemical and electrochemical properties of the synthesized membranes as a function of processing conditions and formulation using a range of microscopic, spectroscopic, and electrochemical techniques. We then integrate select composite membranes into a single electrolyte flow cell configuration and perform polarization measurements with different redox electrolyte compositions. We find that mechanically robust, chemically stable LATP/PVDF composites can support > 40 mA cm^{-2} at 400 mV cell overpotential, but further improvements are needed in selectivity. The insights gained through this work begin to establish the foundational knowledge needed to advance composite polymer-inorganic membranes/separators for NAqRFBs.

Keywords: Redox flow batteries, lithium super ionic conductor, composite polymer-ceramic membranes, nonaqueous electrochemistry

1. Introduction

Redox flow batteries (RFBs) are a promising electrochemical technology suitable for long-duration stationary energy storage due to its decoupled power and energy scaling, long service life, and modularity.¹⁻³ While a diverse array of chemistries have been explored over the past 50 years, current state-of-the-art systems are primarily based on transition metal salts (e.g. vanadium, iron, chromium) dissolved in acidic aqueous electrolytes. However, there is a need to reduce system costs to meet a broader portfolio of grid services, which, in turn, motivates research into alternative chemistries, reactor designs, and separation strategies. An emerging class of RFBs are those utilizing nonaqueous chemistries, as their electrolytes offer extended windows of electrochemical stability and the possibility of using redox couples that are infeasible in aqueous electrolytes due to their stability, solubility, or redox potential. Consequently, nonaqueous redox flow batteries (NAqRFBs) may enable lower system costs through increased energy density, unlocking new routes toward economically viable RFB systems.⁴⁻⁷ Despite this intriguing possibility, current NAqRFB prototypes display limited performance and lifetime due, at least in part, to the lack of membranes with suitable combinations of selectivity, conductivity, and stability.⁸⁻¹¹

Ideally, a RFB membrane should simultaneously block undesired transport of redox-active species and solvent between the positive and negative electrolytes, promote the rapid and selective transport of supporting ions, possess high mechanical and chemical stability, and be conducive to low-cost and scalable production.¹² In practice, this is difficult to implement, and while there have been considerable efforts dedicated to advancing redox chemistries for NAqRFBs, thus far, fewer attempts have focused on developing membranes to support leading chemistries, frustrating full cell performance and durability.⁸⁻¹¹ Most prior research on NAqRFBs incorporates commercially

available ion-exchange membranes,^{13,14} which are not specifically engineered for nonaqueous electrochemical environments and thus typically display unfavorable combinations of ionic conductivity and species selectivity.¹⁵⁻¹⁷ Therefore, new separation approaches must be considered, with particular emphasis on materials developed for energy storage technologies that operate in similar (electro)chemical environments. To this end, the extensive body of knowledge generated from research and development of separators and membranes for Li-ion batteries may inform NAqRFB systems.¹⁸ Notably, low-porosity ceramic conductors, which selectively transport a single ion (e.g., Li⁺, Na⁺) through a stationary solid phase, provide an ideal selectivity and have been explored in several aqueous RFB studies.^{19,20} However, to enable sufficiently low area-specific resistance, the ceramic layer must be exceedingly thin (~10-30 μm), ultimately diminishing the structural integrity necessary to withstand compression in redox flow cells.²¹ The ceramic structure can be made thinner and more flexible by incorporating the solid ion conductor into a polymer matrix, forming a hybrid membrane which can maintain conductance without fracturing.^{22,23} Such a membrane may effectively leverage the perfect selectivity of the ceramic along with moderate area-specific resistance and a dimensionally-stable, flexible structure.

As schematically illustrated in Figure 1, achieving a balance of ionic conductivity, selectivity toward certain ions (i.e., charge balancing ions), and mechanical flexibility are key goals when designing a composite polymer-ceramic membrane. Incorporating polyvinylidene fluoride (PVDF) as the polymeric matrix enables greater mechanical flexibility (i.e., maintaining dimensional stability when it bends or compresses); however, the polymer itself does not contribute to the ionic conductivity or selectivity needed for a performance membrane. In contrast, single-ion conductors (ceramic) have a crystalline structure, resulting in limited mechanical

flexibility and potentially lower the desirable ionic conductivity albeit with perfect selectivity. Therefore, to achieve mechanical flexibility and ionic conductivity while maintaining selectivity, the design and synthesis of ceramic-polymer composites is of significant interest.^{20,24} To increase the ionic conductivity, select salts can also be blended into the hybrid structure as schematically shown in Figure 1. It should be noted that preparing a composite structure using the ceramic-polymer-salt mixture may compromise selectivity wherein the final membrane structure is permeable to certain small molecules. For instance, as shown in Figure 1, a composite ceramic-salt-polymer structure (labeled as hybrid in Figure 1) can provide sufficient mechanical flexibility but imperfect selectivity towards charge balancing ions (in this case, Li^+), allowing for some undesired transport of the redox species (e.g., (2,2,6,6-tetramethylpiperidin-1-yl)oxyl (TEMPO)) through the structure.

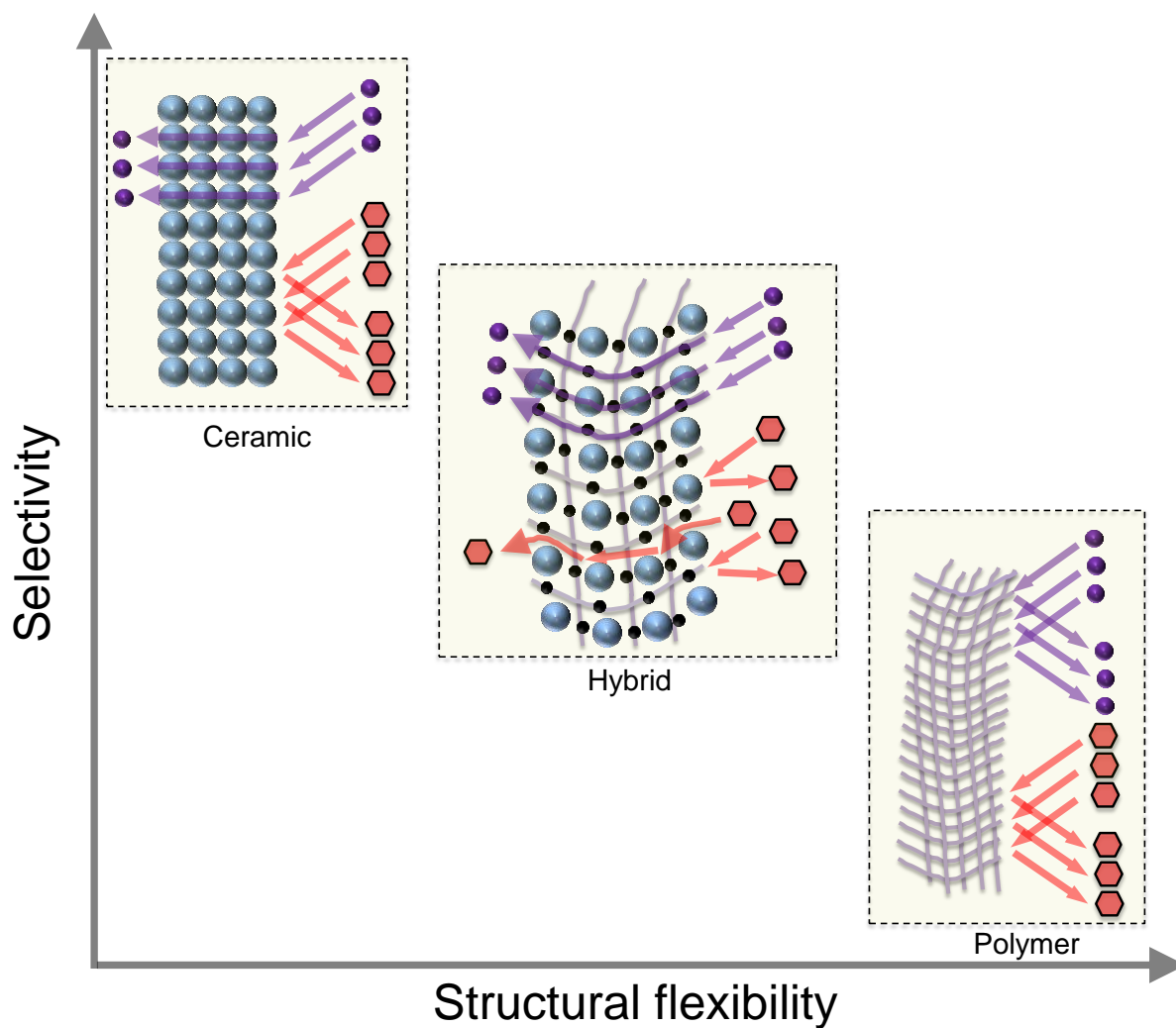



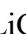



Figure 1. Design features for various configurations of composite structure including polymer (e.g., PVDF), ceramic (e.g., LATP or LAGTP), and hybrid (i.e., composite ceramic-salt-polymer). In the figure, the following symbols have been used; PVDF: , LATP or LAGTP: , LiClO_4 : , Li^+ : , and redox-active species (e.g., TEMPO): .

Here, we explore composite polymer–inorganic membranes for NAqRFBs where Li^+ is the charge-balancing ion. Specifically, we study two different ceramic compounds, $\text{Li}_{1.3}\text{Al}_{0.3}\text{Ti}_{1.7}(\text{PO}_4)_3$ (LATP) and $\text{Li}_{1.4}\text{Al}_{0.4}\text{Ge}_{0.2}\text{Ti}_{1.4}(\text{PO}_4)_3$ (LAGTP), which are blended with PVDF as the polymeric matrix. We first discuss processing factors that contribute to membrane formation, including carrier solvent selection, casting solution composition, substrate treatment, drying conditions, and component fractions. We then characterize the microstructure of various composite ceramic-polymer membranes using optical and scanning-electron microscopy (SEM) and assess the electrochemical stability of as-prepared membranes using coin cell configurations with Li electrodes. Additionally, we blend other common additives (i.e., lithium salts) into the composites and analyzed their impact on the mechanical stability and electrochemical performance. Finally, we evaluate the DC polarization associated with the composite membranes using a single electrolyte flow cell architecture and quantify the crossover of redox-active species for the most promising composite structures. Overall, this study serves as an initial effort toward developing composite polymer-ceramic membranes for NAqRFB systems and may serve as a basis for further exploration of such membranes in RFB technologies.

2. Experimental

2.1. Composite polymer-ceramic membrane preparation

Ceramic pellets of LATP and LAGTP were prepared through a solid-state reaction.²⁵ Lithium carbonate (Li_2CO_3 , $\geq 99\%$, Sigma-Aldrich), ammonium dihydrogen phosphate ($\text{NH}_4\text{H}_2\text{PO}_4$, $\geq 98\%$, Alfa Aesar), aluminum nitrate ($\text{Al}(\text{NO}_3)_3 \cdot 9\text{H}_2\text{O}$, $\geq 97\%$, RusChem), germanium(IV) oxide (GeO_2 , $\geq 99.99\%$, Sigma-Aldrich), and titanium(IV) oxide (TiO_2 , $\geq 99.5\%$, Sigma-Aldrich) were used for preparation of LATP and LAGTP powder. First, $\text{Al}(\text{NO}_3)_3 \cdot 9\text{H}_2\text{O}$ was decomposed to Al_2O_3 by

calcining at 900 °C for 2 h; the procedure was carried out in a muffle furnace with ventilation. Subsequently, Al₂O₃ was mixed with other reagents to fabricate the final compound. To compensate for the lithium losses triggered by the high temperature, 5% stoichiometric excess Li₂CO₃ was supplied.

The proceeding solid-state synthesis was performed in two major sub-steps. First, all the necessary precursors were milled manually with an agate mortar for 15 min or until the ceramic particles were visually uniform. Subsequently, the resulting powder was placed into an alumina crucible lined with a combustible parchment separator so the powder would not stick to the crucible. The sample was then annealed (Nabertherm L5/12/P330 muffle furnace) by heating to 750 °C over 14 h (ramp rate of 0.86 °C min⁻¹), holding at 750 °C for 3 h, and subsequently quenching with air. This step corresponds to the start of rhombohedral NASICON-phase (NASICON: sodium (Na) Super Ionic CONductor) formation. A self-standing porous solid was then taken out of the crucible after cooling, crushed, and milled manually with an agate mortar until a homogeneous blend of ceramic particles was achieved (~15 min). After that, a PEG/acetone solution was added so that the sample gained 3 wt.% of PEG-1500, which improved the formation of the pellets. The suspension obtained was milled continuously with an agate mortar until completely dry. The resulting fine powder was then pressed into pellets ($m = 250 \pm 5$ mg) using a 1 cm diameter press-form (Carver 4350.L hydraulic press) at an applied pressure of ca. 1000 psi. The pellets were then placed into alumina crucibles and annealed by heating the sample to 850 °C over 11 h (ramp rate of 1.25 °C min⁻¹), holding the same temperature for 3 h, and then quenching with air. This resulted in the complete formation of the NASICON phase. For storage, the pellets

were broken into smaller pieces, dried using a vacuum flask, sealed in pouches, and finally stored inside an argon-filled (O_2 , $H_2O < 10$ ppm) glovebox (Inert Technology).

Immediately before composite membrane synthesis, the pre-milled ceramic powder was placed into an agate vial with a single agate 10 mm ball, sealed, and intensively milled for 1.5 h using a high-energy Shaker Mill SPEX 8000 (LabX Inc., USA). The resulting powder was immediately used for membrane preparation. The schematic illustration of the overall synthesis procedure for the composite ceramic-polymer membranes is shown in Figure 2. The composite membranes were synthesized *via* tape-casting using polyvinylidene fluoride (PVDF, average $M_w \sim 534,000$ by GPC, Sigma-Aldrich), lithium perchlorate ($LiClO_4$, $\geq 99.99\%$, Sigma-Aldrich), ceramic powders (as-prepared LATP or LAGTP) and dimethylformamide (DMF, $\geq 99.8\%$, Sigma-Aldrich) as a carrier solvent. The final membrane compositions were 44 wt.% LATP (or LAGTP)-7.5 wt.% $LiClO_4$ -48.5 wt.% PVDF and 44 wt.% LATP (or LAGTP)-56 wt.% PVDF further denoted as LATP/ $LiClO_4$ /PVDF (LAGTP/ $LiClO_4$ /PVDF) and LATP/PVDF (LAGTP/PVDF), respectively. The ceramic and lithium salt fraction used in the composites were estimated in preliminary tests (*vide infra*) to yield a suitable composite membrane. The solutions for the tape casting were prepared by the following approach:

1. Dissolution of PVDF in DMF at 60 °C with mild stirring (400 rpm).
2. Addition of composite components, $LiClO_4$ and/or milled ceramics, followed by intense stirring (1400 rpm) for 5 h at 60 °C.
3. Degassing for 24 h without added heat. The solution was stagnant to allow for the removal of bubbles introduced by stirring; sedimentation was not observed under such conditions.

The solution was subsequently cast onto a plasma-treated glass plate using a doctor blade (blade gap: 200 μm ; speed: 15 mm min^{-1} ; temperature of substrate: $\sim 70\text{ }^\circ\text{C}$). The freshly deposited membrane was immediately put into a vacuum oven (with vacuum pressure up to 70 mbar) at 80 $^\circ\text{C}$ for 1 h. As-synthesized membranes were either used for analysis or sealed in pouches.

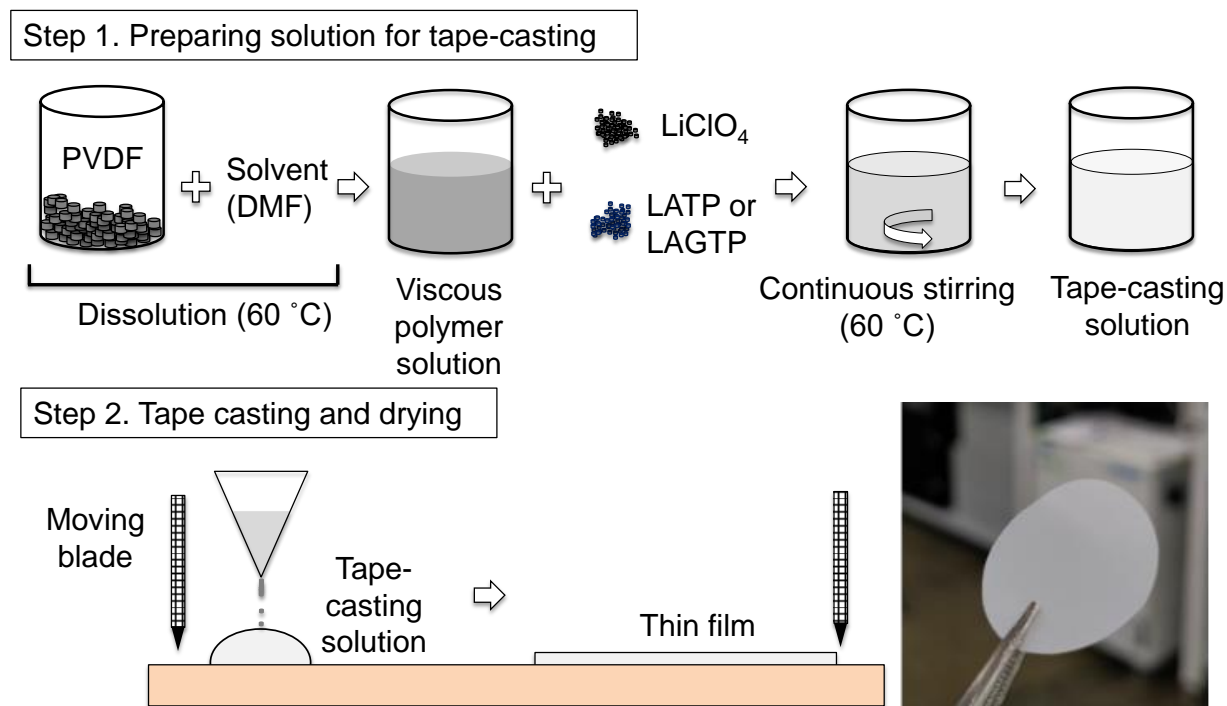


Figure 2. Schematic illustration of the synthesis procedure for the composite membranes.

2.2. *Ex situ* characterization of composite membranes

The membrane electronic conductivity was measured by DC polarization using a Metrohm Autolab galvanostat/potentiostat (fixed potential of 0.5 V for 2 h with 20 s interval of recording) using an in-house symmetric cell with copper electrodes (detailed in Ref. 26). The conductivity

measurements were performed under dry conditions (i.e., no electrolyte) as described in the Supporting Information (see Figure S1).

The membrane electrochemical stability window (ESW) was measured (in dry conditions) by linear sweep voltammetry in a Li/stainless steel (SS) coin cell using a Metrohm Autolab galvanostat/potentiostat (voltage range 2 – 6 V vs Li/Li⁺). For the ESW measurements, Li and SS were used as the counter and working electrodes, respectively. The ESW for the as-prepared coin cells is provided in Figure S2. To explore the stability of the composite membrane and constituent components towards the electrolytes used in flow cell experiments, PVDF, LATP/LiClO₄/PVDF, and LATP/PVDF were soaked for 24 h in acetonitrile (ACN, purity >99%, Alfa Aesar) or propylene carbonate (PC, purity >99%, Alfa Aesar) solutions. Stability was estimated as a mass loss of membrane after drying in vacuum oven for 1 and 20 h (for ACN and PC, respectively).

A scanning electron microscope (FEI Versa 3D™ DualBeam™ system) was used for imaging the composite membranes. Experiments were performed in a secondary electron (SE) mode at 10 kV at sample tilts of 0 – 45 degrees. To study the membrane cross-sections (fracture surface morphology), samples were cooled under flowing liquid nitrogen (at -196 °C) and then immediately fractured by tweezers into two halves to form a clean crack.²⁷

To assess the selectivity of the composite membranes toward the electroactive species, concentration-gradient induced crossover measurements were conducted using the H-cell setup shown schematically in Figure S3. 2,2,6,6-tetramethylpiperidin-1-yl)oxyl (TEMPO, 98%, Alfa Aesar) was used as-received for preparing the TEMPO-rich solution where 0.5 M TEMPO along

with 0.5 M lithium bis(trifluoromethanesulfonyl)imide (LiTFSI, 99.99%, Alfa Aesar) was dissolved in ACN (99.98%, BASF). In the other side of the H-cell (TEMPO-deficient electrolyte) the solution only contained 1 M LiTFSI dissolved in ACN. The as-prepared composite membranes were placed between the two solutions within the H-cell and using cyclic voltammetry (see Figure S3), the concentration of TEMPO in the TEMPO-deficient electrolyte was measured over an extended time and the permeability of the composite membrane was quantified following a procedure described elsewhere.²⁸ Cyclic voltammetry measurements were performed on a Bio-Logic VMP-3 potentiostat at 10 mV s⁻¹ using a glassy carbon working electrode (BASi, 3.0 mm diameter), Pt coil counter electrode (BASi, 99.95%), and fritted Ag/AgCl reference electrode (BASi).

2.3. Flow cell experiments

Electrolyte preparation, cell assembly, and flow cell experiments were performed in an argon-filled glove box (Inert Technologies, 4GB 2500, O₂ <5 ppm, H₂O <1 ppm). TEMPO was used as-received, and to prepare the oxidized form of TEMPO (2,2,6,6-Tetramethyl-1-piperidinyloxy-oxo tetrafluoroborate or TEMPO-BF₄), a chemical oxidation procedure was adopted based on previous work.²⁹ In brief, TEMPO (11 g) was dissolved in acetonitrile, and nitrosonium tetrafluoroborate (NOBF₄, 98%, Alfa Aesar, 1.1 molar equivalents) was added gradually. Subsequently, the solution was removed from the glovebox and transferred to a rotary evaporator (Buchi R210) to remove excess solvent; TEMPO-BF₄ was recovered and collected as a solid, orange powder. For all flow cell experiments conducted in this work, the electrolyte composition included 0.25 M TEMPO and 0.25 M TEMPO-BF₄ with 1 M LiTFSI supporting salt dissolved in either ACN (≥99%, Alfa Aesar) or PC (≥99%, Alfa Aesar).

A graphical representation of the experimental setup used in this work is provided in Figure 3. Note that all flow cell experiments were performed using a single electrolyte configuration to maintain a constant state of charge (SoC) throughout polarization testing.³⁰ The flow cell architecture comprised interdigitated flow fields machined on impregnated graphite (G347B graphite, MWI Inc.), polypropylene flow diffusers (Adaptive Engineering), and an as-prepared composite polymer-ceramic membrane sandwiched between the positive and negative electrodes. Polytetrafluoroethylene (PTFE) gaskets were used in the negative and positive sides for sealing the electrolyte and providing the required compression. A single layer of as-received carbon felt (AvCarb Material Solutions, model: G300A) with a projected area of 2.55 cm² (1.7 × 1.5 cm) was utilized for both the negative and positive sides, and each electrode was compressed by ~25% of its initial nominal thickness (~3.4 mm).

To conduct cell testing, the electrolyte was pumped from a hermetically sealed perfluoroalkoxy alkane (PFA) jar (10 mL, Savillex) to the cell through Masterflex® Norprene® tubing (Size: L/S 14, Cole Parmer, USA) using a Masterflex® peristaltic pump (Cole Parmer, USA). Following pump calibration and before collecting any data, the flow cells were conditioned by circulating the electrolyte through the reactors at 5 mL min⁻¹ for 15 min, followed by a cell potential hold at 50 mV for 30 min to remove any bubbles trapped inside the electrodes and to ensure adequate wetting of the cell components. Subsequently, a constant flow rate of 25 mL min⁻¹ was used for circulating the electrolyte in all experiments. A Bio-Logic VMP-3 potentiostat was employed for conducting polarization and electrochemical impedance spectroscopy (EIS). The polarization measurements were performed by applying voltages ranging from 0 to 400 mV (interval of 50 mV), holding the

potential constant for 5 min at each step and recording the corresponding current (last 40% of the recorded data arithmetically averaged). The AC electrochemical impedance spectroscopy experiments were performed at open circuit voltage with a 5 mV perturbation amplitude within the frequency range of 200 kHz – 10 mHz.

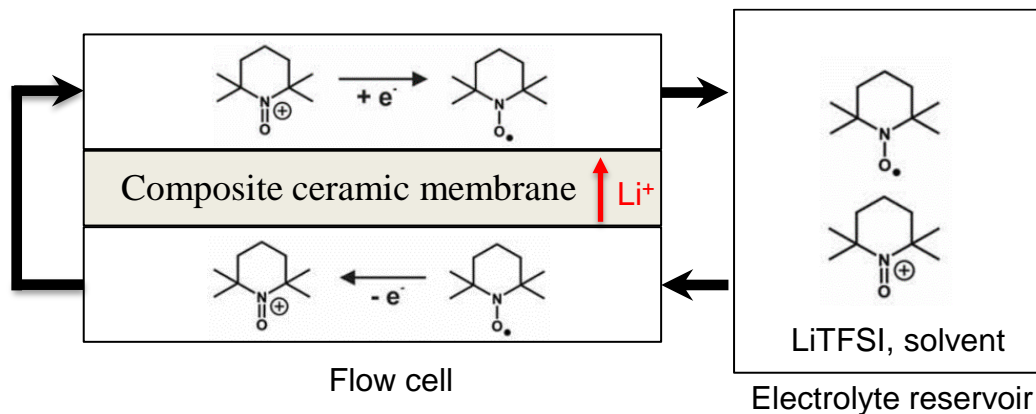


Figure 3. Single electrolyte flow cell setup utilizing TEMPO (0.25 M) and TEMPO-BF₄ (0.25 M) as the redox active material in electrolytes containing 1 M LiTFSI dissolved in either ACN or PC.

3. Results and Discussion

3.1. Composite membrane preparation procedure

We synthesized the composite membranes used in this work by initially refining the procedures for both the ceramic filler and polymer film. Here, we focus on the preparation of the PVDF film, as we have described LATP synthesis elsewhere.^{25,31} The target polymer film should ideally be thin (<25 μm) with low porosity (<25%) and uniform surfaces. To identify suitable conditions for membrane preparation, we varied the casting conditions as follows: *selecting a suitable solvent* → *achieving a uniform membrane thickness* → *selecting an appropriate casting conditions* → *drying*

the samples → *controlling additional minor variations*. We expand on these respective steps below.

N,N-dimethylformamide (DMF) was chosen as the solvent for polymer dissolution. Among other candidate solvents (i.e., acetone, dimethylsulfoxide, N-methyl-2-pyrrolidone), DMF has a high boiling point (153 °C), completely dissolves PVDF, and slowly absorbs water from the atmosphere, allowing membrane synthesis in air. The PVDF film thickness was tuned by adjusting the viscosity of the suspension through the DMF:PVDF mass ratio. Figure S4(a) shows the dependence of PVDF weight fraction (wt.%) in the DMF:PVDF suspension on the final thickness of the PVDF membrane, which can be adjusted within the range of 8 – 20 μm by varying the composition of the casting solution. We note that suspensions with PVDF wt.% less than 8 or higher than 20 (not shown in the figure) are unsuitable for casting. When the PVDF concentration was < 8 wt.% (ca. 200 mPa s), the resulting film was too thin and brittle, whereas if the PVDF concentration was > 20 wt.%, the suspension became too viscous (> 2000 mPa s). Considering these factors, the 85:15 wt.% DMF:PVDF suspension composition was chosen, assuring high mechanical stability under suitable processing conditions.

Selecting appropriate casting conditions necessitates proper treatment of the substrate (support) prior to casting the suspension. Without effective substrate treatment, a horizontal inhomogeneity of the film will be observed (Figure S4(b)). One method to suppress this effect is to improve adhesion between the film and substrate. For example, since we used quartz glass as a casting support, we can improve adhesion by activating the glass surface and removing organic contaminants. To this end, we subjected the substrate to variable combinations of solvent washing,

ultrasonic treatment, and air plasma quenching (Diener, Atto plasma cleaner), which are summarized in Table S1. The effectiveness of the glass treatment was assessed by measuring the contact angle between the substrate and deionized water as well as the porosity of the polymer film. In general, lower contact angles indicate fewer undesired organic impurities, facilitating more uniform film formation and yielding lower porosity. The contact angle measurements were performed using a DSA100 Drop Shape Analyzer (Krüss Scientific, Germany). The best polymer characteristics (i.e., those with the lowest porosity, as formulated in Equation S2) are achieved when the glass is washed with acetone, dried under inert gas (argon), and subjected to plasma treatment immediately before membrane casting. The resulting porosity was ~40%.

To further decrease the porosity, the drying conditions of the suspension were refined by adjusting the temperature and pressure of the vacuum chamber. At temperatures well above the glass transition temperature (-35 °C), polymer chains can rearrange, aligning the polymer structure and decreasing porosity;³² the dynamic vacuum, in turn, increases solvent evaporation rates from the suspension. However, this procedure can be too aggressive, as the dynamic vacuum more rapidly volatilizes solvent from the suspension, leaving behind void space and thus stimulating pore formation within the membrane. To explore this possibility, SEM images of the membranes were taken at different drying conditions (Figure 4): 80 °C + atmospheric pressure (*only T*); 80 °C + dynamic vacuum (*T+vac*); 25 °C + dynamic vacuum (*only vac*). As illustrated in Figure 4, the porosity of the membranes increases in the following order: *only T* ≤ *T+vac* << *only vac*. The membranes dried with just vacuum are unusable due to the presence of multiple pores throughout the composite structure (see Figure 4(d)); *Only T* and *T+vac* conditions were deemed acceptable

and can be selected based on the desired membrane porosity (< 25%). We opted to examine $T+vac$ in this work.

To finalize the preparation of pure PVDF films, we varied additional minor conditions, including the speed of the casting blade, the temperature of the glass substrates, and time and temperature of the suspension degassing, among other factors. We achieved the previously stated desired PVDF film characteristics: controllable <20 μm thickness, uniform structure, and porosity less than 25%, which allowed us to continue formation of the LATP/PVDF (LAGTP/PVDF) and LATP/LiClO₄/PVDF (LAGTP/LiClO₄/PVDF) composite membranes.

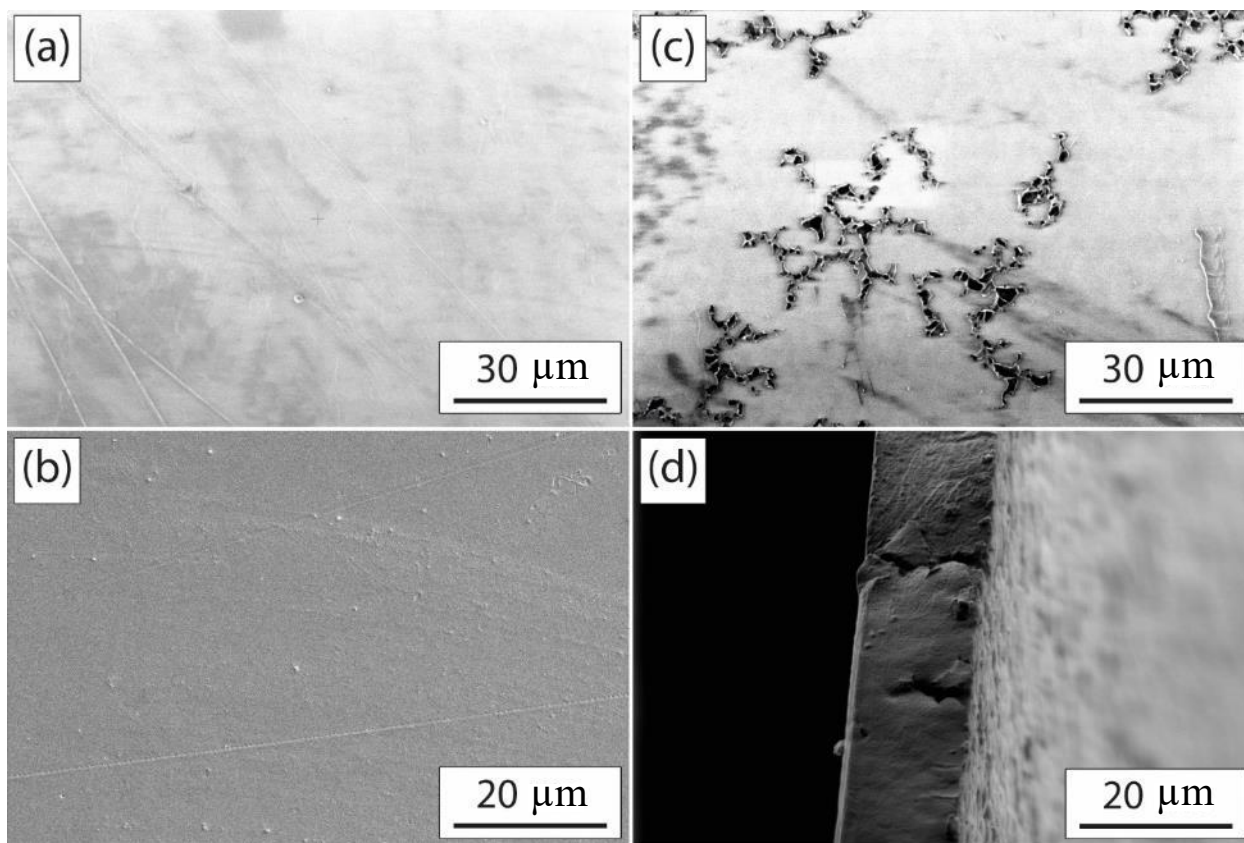


Figure 4. SEM images of PVDF membranes dried in different conditions – (a) *only T*, (b) *T+vac*, and (c) *only vac*. (d) Cross-section of the membrane dried with only vacuum illustrating the presence of “end-to-end” pores.

After the preliminary polymer casting optimization, we studied the appropriate composite synthesis conditions for the ceramic. Besides the polymer requirements achieved above, the final composite membrane should contain a suitable fraction of inorganic components, possess low particle size with a narrow distribution, and maintain flexibility and mechanical stability. In general, the greater the fraction of conductive ceramic (e.g., LATP) in the sample, the higher the ionic conductivity of the membrane. This is achieved through the percolation effect—pathways of ceramic particles align themselves throughout the membrane to enable Li^+ transport. However, we found that composite membranes with LATP content greater than 44 wt.% were challenging to synthesize as the suspensions from which they were casted were too viscous and the products were difficult to handle post-synthesis, as the composites were too brittle. As such, we studied membranes with the maximum achievable ceramic composition (44 wt.%).

We also explored the addition of various lithium salts (e.g., LiClO_4 , LiTFSI, lithium tetrafluoroborate) to enhance ionic conductivity, as has been already demonstrated for both neat polymers and ceramic-polymer composites.³³⁻³⁵ An optimal material ratio was found by relating the number of Li^+ ions to the number of polymer chains or functional groups (e.g., oxygens in polyethylene oxide). In the case of the LATP/ LiClO_4 /PVDF membrane we studied, the amount of Li^+ from dissolved LiClO_4 was correlated with the number of fluorine atoms in PVDF; a

concentration of 7.5 wt.% LiClO₄ was chosen, corresponding approximately to a 4:1 ratio of Li⁺ to F.

Lastly, suitable conditions for LATP in the composite were examined by comparing hand-milling of LATP powder in an agate mortar with ball milling (SPEX ball mill 8000); the mean particle size and size distribution were measured using a Fritsch Particle Analyzer (FRITSCH, Idar-Oberstein, Germany). Figure 5(a) illustrates the mean particle size of LATP as a function of milling time. After 90 min of ball milling, the mean particle size was ~1 μm and the spread was 0.2 – 1.1 μm, as shown in the histogram in Figure 5(b); as such, we determined that 90 min is a reasonable milling time to balance diminishing returns on particle size with increases in processing time. We note that in Figure 5(a), “0 min” corresponds to hand-milling of LATP in the mortar.

By developing all synthesis steps separately, we obtained composite membranes with suitable composition and physical and mechanical properties. The LATP/PVDF, LAGTP/PVDF, LATP/LiClO₄/PVDF, and LAGTP/LiClO₄/PVDF composite membranes prepared by this methodology were further characterized via physical and electrochemical methods to evaluate their performance.

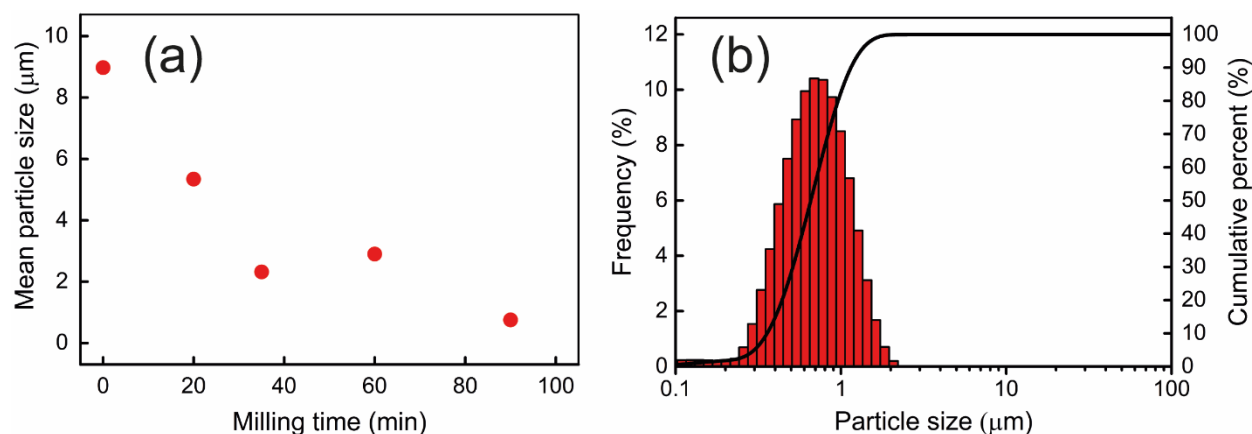


Figure 5(a). Dependence of the mean particle size of LATP on milling time in the shaker, and 5(b). Particle size distribution histogram of LATP milled for 90 min in the shaker.

3.2. Microscopy and *ex situ* electrochemical characterization

After exploring and developing the synthetic procedure for the composite membranes, we studied the membrane morphology using SEM. As an example, Figure 6 shows SEM images of both the neat polymer (PVDF) and LATP/PVDF membranes. Due to the tape casting process, there are two disparate sides of membrane—a rough side that was in contact with air while drying (Figure 6(a)) and a smooth side that was in contact with the support (Figure 6(b)). Cross-sectional SEM images of the PVDF membrane reveal a dense structure with no micron-scale porosity connecting the two faces (Figure 6(c)). Cross-sectional SEM also confirms the presence of embedded LATP particles within the PVDF matrix for composite membrane samples, varying in size (1 – 20 μm) and spatial distribution (Figure 6(d)-(f)). Despite the narrow particle size distribution, some agglomeration of the inorganic components can be observed, which likely arises during tape casting from the suspension. With the addition of ceramic microparticles for the formation of LATP/PVDF, a small increase in the porosity (Figure 6(d)-(e)) was realized, especially for the rough side of the membrane. The cross-sectional image of the composite LATP/PVDF membrane (Figure 6(f)) demonstrates tight contact between polymer and ceramic

components, indicating that the ceramic LATP and LAGTP are closely bound to the membrane structure. While these images provide evidence of increased porosity, SEM only allows for surface level observation of the porosity, with no further indication of pore connectivity or percolation networks through the interior of the membrane, necessitating additional morphological (e.g., X-ray tomography) electrochemical (e.g., conductivity analysis), and transport characterizations (e.g., permeability analysis).

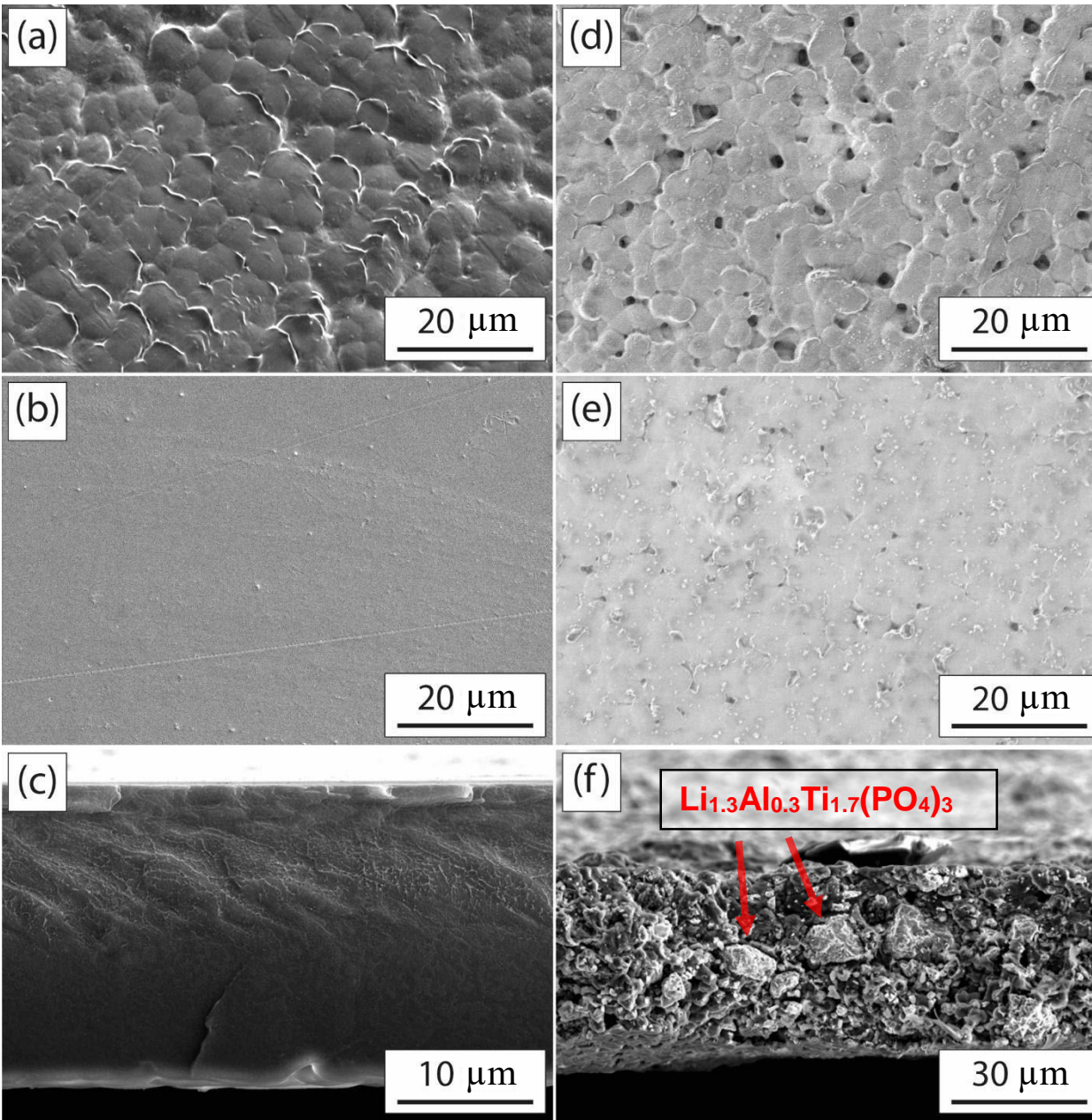


Figure 6. SEM micrographs of PVDF membrane—(a) side facing air during casting (rougher structure), (b) side facing the substrate during casting (finer/smooth structure), (c) cross-section—and of composite LATP/PVDF membrane—(d) rougher side, (e) smoother side, (f) cross-section.

To understand the feasibility of these membranes for flow cell operation, we performed electrochemical characterizations using as-prepared composite membranes. Given the key role of the ceramic structure on lithium-ion conductivity, LAGTP was used in addition to LATP for preparing the composite structures. The synthesis procedure remained unchanged (Figure 2), and different configurations of the composite structures were prepared including LATP/LiClO₄/PVDF, LATP/PVDF, and LAGTP/PVDF composites. Given the difference between the ceramic structure of LATP and LAGTP (in solid state), it is of interest to explore how such a difference in the ceramic structure influences the performance of flow cells with electrolytes including organic molecules.

For this purpose, we measured the ionic conductivity (σ_i), electronic conductivity (σ_e), and ESW of the membranes using electrochemical impedance spectroscopy in flow cell conditions with ACN (Figure 3), DC polarization in a dry symmetric cell, and linear sweep voltammetry in dry coin cells, respectively. The resulting data is presented in Table 1. All composite membranes appeared stable in the potential range of 2.2 – 4.5 V vs Li/Li⁺ and demonstrated low electronic conductivity ($\sigma_e < 10^{-6}$ mS cm⁻¹) in all cases, suggesting they are sufficiently insulating to prevent short-circuiting between the electrodes within the cell.

Table 1. Composite ceramic-polymer *ex situ* characterization

Membrane	Dry Thickness (μm)	Ionic conductivity, (mS cm^{-1})	ESW, vs. Li/Li ⁺ (V)	Electronic conductivity, (mS cm^{-1})
LATP/LiClO ₄ /PVDF	35-45	2.1 ± 0.1	2.0-4.5	$< 10^{-6}$
LATP/PVDF		0.8 ± 0.1	2.0-4.8	$< 10^{-9}$
LAGTP/PVDF		0.6 ± 0.1	2.0-4.8	$< 10^{-9}$

Finally, to ensure the stability of the composite membranes in the electrolyte environment, we performed soaking tests, where we measured the change in mass following 24 h of exposure to various electrolyte compositions. Each membrane sample was first weighed and then soaked separately in ACN, PC, 0.5 M TEMPO in ACN, or 0.5 M TEMPO in PC, then dried at 60 °C under dynamic vacuum for 12 h before weighing again to estimate mass loss. The results in Table S2 show that PVDF and LATP/PVDF were sufficiently stable toward each of the target electrolyte components, but LATP/LiClO₄/PVDF was not, which lost approximately 13 wt.% in all soaking solutions (*vide infra*).

3.3. Flow battery analysis

To demonstrate the efficacy of these membranes in a RFB, we employed a single electrolyte flow cell architecture (Figure 3) using a model redox couple, TEMPO/TEMPO-BF₄, which exhibits facile kinetics and high molecular stability.³⁶⁻³⁸ Adopting such a diagnostic cell configuration enables a relatively straightforward assessment of the influence of the composite polymer-ceramic membrane structure on the overall cell performance. Further, this cell design

eliminates complications stemmed from unwanted species transport through the membrane (i.e., crossover) and maintains a constant state of charge throughout the entire experiment, whereas similar analyses in commonly used full cell setups may be cumbersome, as variations in the state of charge, along with possible crossover of redox-active species, can substantially influence polarization behavior. The use of TEMPO/TEMPO-BF₄ also minimizes the impact of electrode kinetics on potential response during polarization, allowing for a simplified measurement of membrane performance without additional corrections. First, we attempted to incorporate membranes containing only PVDF within the flow cells; however, we found the pure PVDF completely stymied cell performance (i.e., zero-current output for increasing cell voltages). As shown through the SEM images in Figure 4, PVDF, despite having high stability in TEMPO-containing solutions (see Table S2), does not form a microporous structure upon casting, and does not demonstrate ion-exchange capability, verifying the impermeable structure in its original morphology, as shown schematically in Figure 1.

Polarization curves associated with the single electrolyte cell containing LATP/LiClO₄/PVDF and LAGTP/LiClO₄/PVDF are shown in Figure 7, comparing the two different solvents used in this work. As evinced by the data, utilizing ACN as the solvent yields significantly improved cell performance, owing to the higher conductivity and lower viscosity of the resulting electrolyte. Specifically, applying 400 mV results in ~10 mA cm⁻² for PC, whereas a similar cell voltage for ACN increases the current density by more than 8-fold (~85 mA cm⁻²).

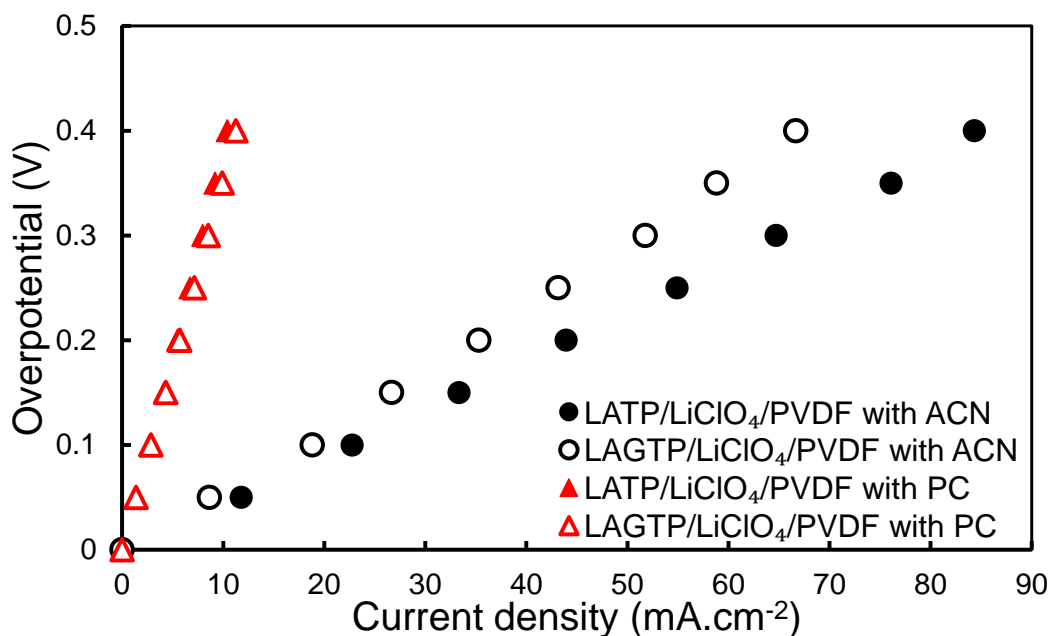


Figure 7. Polarization profiles for composite polymer-ceramic membranes, LATP/LiClO₄/PVDF and LAGTP/LiClO₄/PVDF, in single electrolyte flow cells with different solvents. Measurements were performed using electrolytes containing 0.25 M TEMPO, 0.25 M TEMPO-BF₄, and 1 M LiTFSI flowing at 25 mL min⁻¹. Potentials were applied in increments of 50 mV for 5 min and measured currents were averaged over the last 2 min.

It is also worth noting that regardless of the solvent used within the electrolyte, the cell current is a linear function of applied voltage. This trend implies that the cell polarization is dominated by ohmic losses across the testing conditions employed in this work, consistent with the expected low kinetic losses associated with TEMPO. Further, while the ohmic voltage losses include losses associated with ion transport through both the electrolyte (i.e., electrolyte ionic resistance) and the membrane, relative changes for a given electrolyte are indicative of variations in membrane properties.

The variations in cell overpotential for different ceramic configurations (LATP and LAGTP) are also illustrated in Figure 7 for both PC and ACN. Employing LATP within the polymer-ceramic composite structure improves the cell performance compared to LAGTP in ACN (~31% higher current at 400 mV), which we tentatively attribute to increased composite polymer ionic conductivity with LATP compared to LAGTP, as tabulated in Table 1. When utilizing PC as the solvent, the cell output current remains $< 15 \text{ mA cm}^{-2}$ (at 400 mV), regardless of the ceramic used within the composite. In this case, the cell polarization is dominated by low ionic conductivity of the electrolyte utilizing PC, meaning that improvements in the ceramic structure do not propagate to significant variations in cell behavior, despite the slightly higher conductivity of LATP compared to LAGTP.¹ To further explore the influence of different composite polymer-ceramic membrane constituents on the observed performance in Figure 7, single electrolyte polarization was repeated for a series of different polymer-ceramic composites.

As schematically shown in Figure 1, the incorporation of the salt (LiClO_4) along with the ceramic within the polymer matrix can in principle improve the ionic conductivity by providing additional pathways for ion transport. To understand its role in cell polarization, three different variations of composite polymer-ceramic membranes were considered (Figure 8); here, the composite membrane including PVDF was blended with 1) only the ceramic (LATP/PVDF, diamonds), 2) only the lithium salt (LiClO_4 /PVDF, squares), or 3) a combination of both the ceramic and lithium salt (LATP/ LiClO_4 /PVDF, circles). The effect of different membrane constituents on the cell performance was repeated for both solvents, ACN (Figure 8(a)) and PC (Figure 8(b)). Regardless of the solvent used, utilizing LiClO_4 within the membrane morphology

substantially improves the cell performance for both composite structures, which demonstrates that blending a lithium salt (e.g., LiClO_4) within the matrix can indeed improve the Li^+ conductivity if the membrane structure remains mechanically robust. However, *post mortem* analyses of the composite ceramic-polymer structures containing LiClO_4 reveal that when lithium salt is blended in the composite structure, the salt (in this case, LiClO_4) dissolves into the electrolyte, leaving several voids in the composite membrane structure, as shown by SEM images in Figure S5. Therefore, despite significant improvements observed in the cell polarization (more than 100% enhancement), the composite ceramic-polymer membrane does not remain stable and thus, the increased microporosity can be assumed to hinder ion selectivity.

Similar stability analyses were also conducted for the other composite membranes, including only PVDF and LATP/PVDF, as shown in Table S2. The mass-uptake analysis confirms that the composite membrane containing only LATP in PVDF remains stable regardless of the electrolyte composition. Therefore, to assure stability, the lithium salt was ultimately removed from the composite membrane structure. As shown in Figure 8(a), the cell discharge current density reaches 40 mA cm^{-2} at 400 mV for the single electrolyte cells utilizing a PVDF matrix blended with LATP. Similar to prior cases, a linear cell polarization is recorded across the range of overpotentials considered in this work, indicating the dominance of the ohmic losses. Indeed, despite having lower cell performance, the LATP/PVDF structure remains mechanically stable throughout testing and does not have the same nonselective micropores created by LiClO_4 leaving the structure. Given the mechanical stability of LATP/PVDF composite membranes in both type of solvents (ACN and PC), it is of interest to further explore the polarization curves and analyze different sources of overpotential for this class of composite membranes.

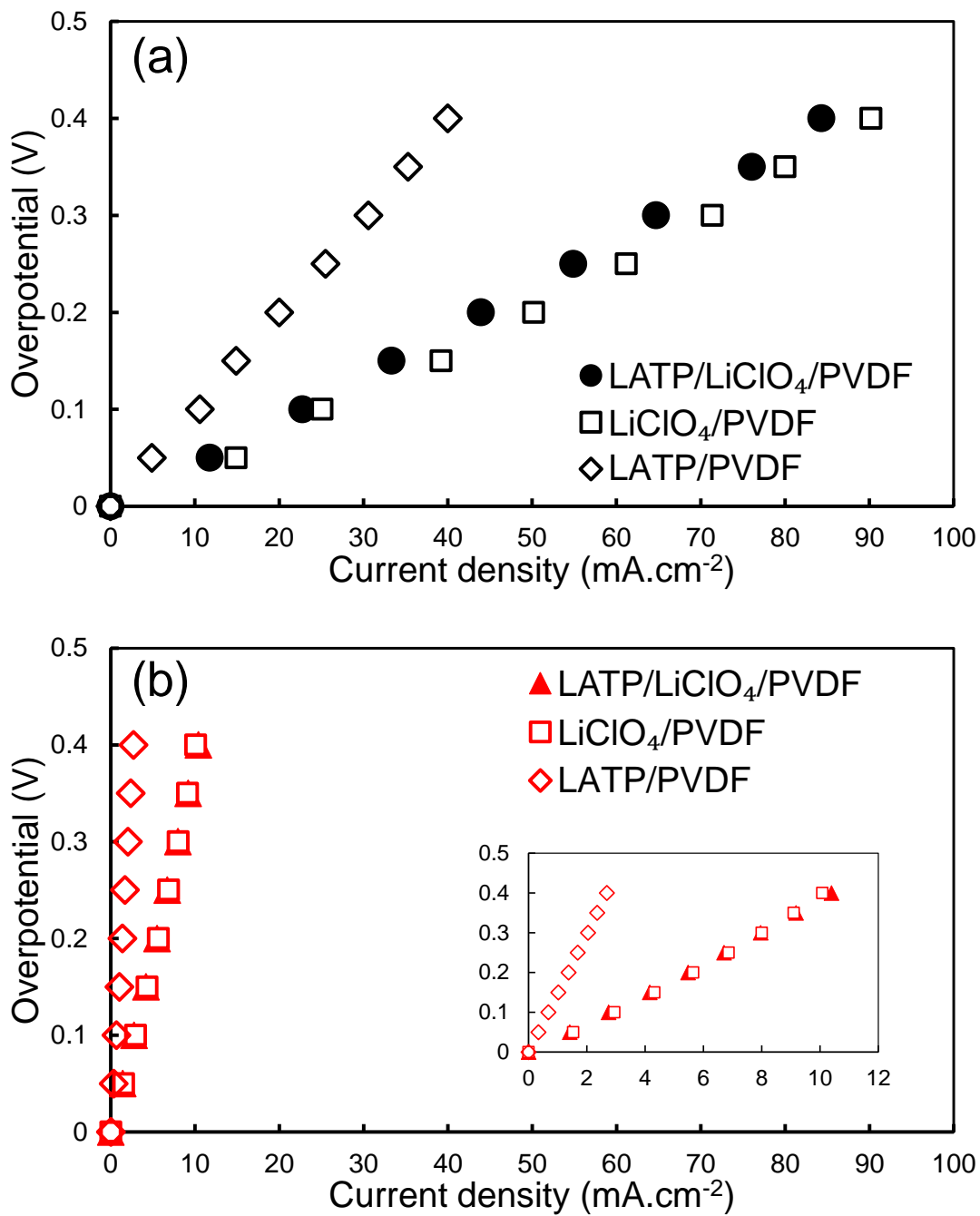


Figure 8. Polarization curves associated with various configurations of composite membranes in single electrolyte flow cells with different solvents; (a) ACN; (b) PC. Measurements were

performed using electrolytes containing 0.25 M TEMPO, 0.25 M TEMPO-BF₄, and 1 M LiTFSI flowing at 25 mL min⁻¹. Potentials were applied in increments of 50 mV for 5 min and measured currents were averaged over the last 2 min.

The IR-corrected and regular polarization curves of LATP/PVDF composite membranes measured with different solvents (maintaining identical electroactive species and supporting salt) are compared in Figure 9 (diamonds have been used for regular polarization data and asterisks for IR-free). The high-frequency x-axis intercept obtained from EIS was used to estimate the ohmic losses for the cell, which includes the resistance to electronic/ionic current stemming from the membrane, electrolyte, electrodes, and all other contact resistances. Subsequently, the IR-corrected curves were assessed by subtracting the voltage losses associated with the ohmic overpotential from the cell voltage such that the IR-free polarization profiles are primarily indicative of kinetic and mass-transport losses associated with the single electrolyte cell. Analyzing the polarization curves for the cells with LATP/PVDF composite membranes (see Figure 9(a) and 9(b)) reveals that regardless of the solvent type, the cell polarization is dominated by the ohmic losses. Even at the highest discharge currents measured with the composite LATP/PVDF membranes (i.e., ~40 mA cm⁻² with ACN (Figure 9(a)) and ~2.6 mA cm⁻² with PC (Figure 9(b))), the combined kinetic and mass transport losses are ~9.7% (with ACN) and ~17.8% (with PC) of the entire cell polarization.

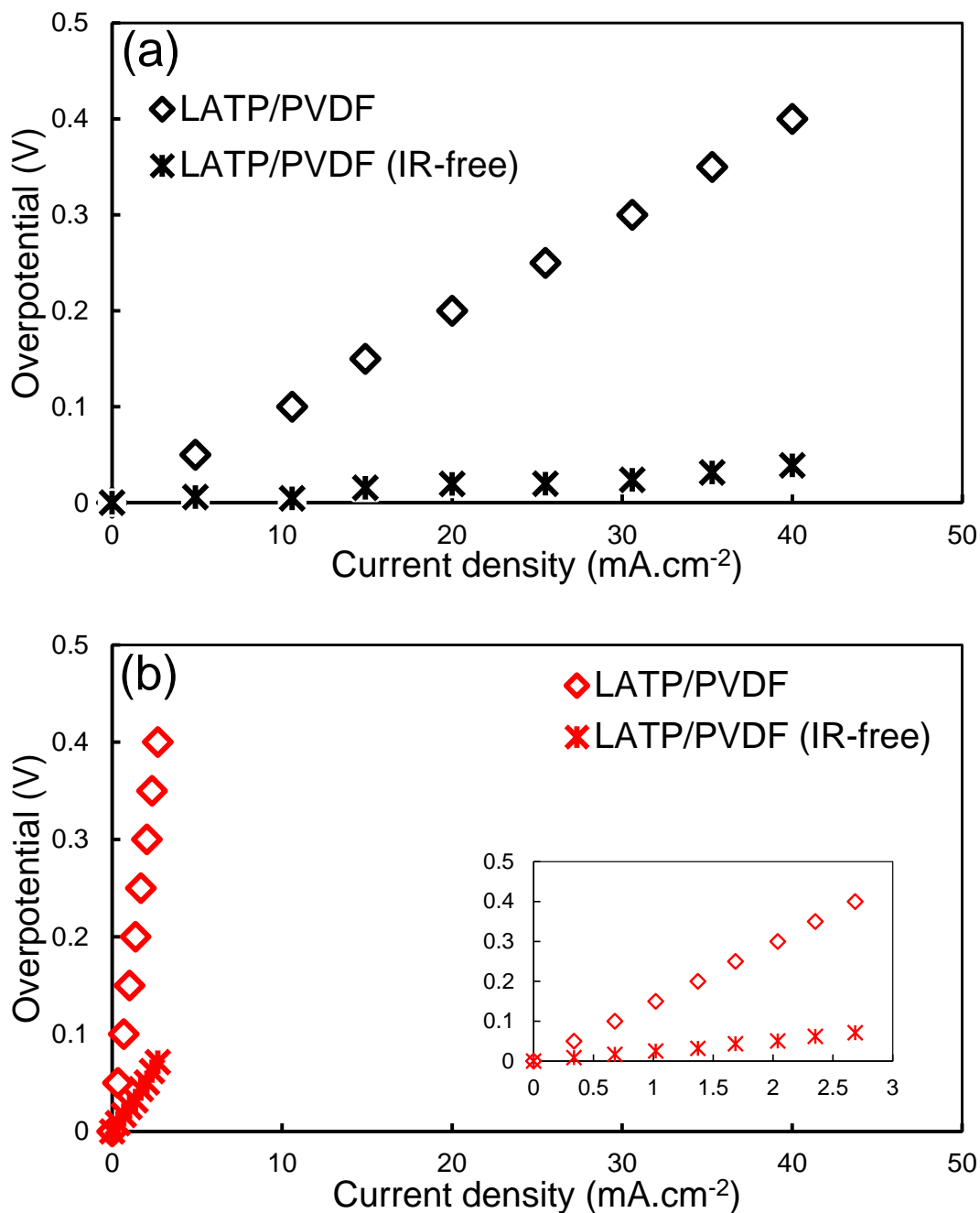


Figure 9. Distribution of different sources of overpotential for single electrolyte flow cells containing (a) ACN and (b) PC. Ohmic losses were estimated from the high-frequency intercept obtained using EIS and subtracted from the total overpotential. Measurements were performed using electrolytes containing 0.25 M TEMPO, 0.25 M TEMPO-BF₄, and 1 M LiTFSI flowing at

25 mL min⁻¹. Potentials were applied in increments of 50 mV for 5 min and measured currents were averaged over the last 2 min.

Finally, it is important to explore the selectivity of the composite LATP/PVDF membranes toward the electroactive species (i.e., TEMPO/TEMPO⁺). Although the crossover of TEMPO/TEMPO⁺ through the membrane would not result in any irreversible capacity loss with the single electrolyte cell configuration considered in this work, for full cell cycling with another active species, such undesired transport of electroactive species would have an impact on the available capacity and coulombic efficiency. To this end, the concentration-gradient induced crossover of TEMPO through the composite LATP/PVDF membrane was explored using the setup shown in Figure S3. As detailed earlier, a TEMPO-rich electrolyte was prepared and placed in one side of the H-cell setup and in the other side (TEMPO-deficient electrolyte) the solution only contained supporting salt dissolved in ACN (see Figure S3 for more details). Followingly, the concentration of TEMPO diffused through the composite LATP/PVDF membrane was quantified (using cyclic voltammetry) within the TEMPO-deficient electrolyte over an extended time and the permeability of the composite membrane was assessed (see Table S3).^{18,39,40} As tabulated in Table S3, the permeability of the LATP/PVDF composite membrane (with respect to TEMPO) was $\sim 2 \times 10^{-6} \text{ cm}^2 \text{ s}^{-1}$. Thus, the composite LATP/PVDF membranes do not exhibit perfect selectivity towards Li⁺. This may appear counterintuitive at first, as incorporating the ceramic particles within the polymer matrix provides a conductive pathway for the lithium ions through the composite LATP/PVDF structure. Since the PVDF structure is not permeable to either lithium ions or TEMPO, incorporating lithium-ion conducting LATP particles is necessary for enabling ionic conductivity within the membrane phase. However, the voids formed within the interface of

ceramic particles and the polymer matrix during the synthesis procedure also provides pathways for TEMPO crossover. Since the structure of composite LATP/PVDF membrane remains intact, the permeability of the LATP/PVDF hybrid membranes can likely be further decreased by engineering the interfacial morphology of the composite structures. Our future works will be dedicated toward engineering the structure of these composite membranes to achieve higher ionic conductivity and selectivity.

4. Conclusions

Various configurations of composite ceramic-polymer membranes were prepared and characterized for Li⁺-conducting NAqRFBs. Synthetic methods for composite polymeric Li⁺-conducting ceramic membranes were demonstrated with few steps and repeatable methodology for several ceramic-polymer morphologies, including LATP/LiClO₄/PVDF and LAGTP/LiClO₄/PVDF. Owing to the simplicity of the tape casting procedure, membrane morphological characteristics were relatively uniform and consistent across the samples studied. Physicochemical and electrochemical characterizations of resultant membranes demonstrated that the composite Li⁺-conducting membranes maintained good mechanical robustness and reasonable conductivities in NAqRFB electrolytes. Single electrolyte flow cells demonstrated polarization behavior in model electrolyte compositions with two different solvents (ACN and PC), with comparable performance between membranes containing embedded NASICON-type particles (LATP and LAGTP) with different host structures. Among various combinations of ceramic-polymer structures, it was shown that the LATP/PVDF composite is capable of delivering > 40 mA cm⁻² at 400 mV cell voltage. The findings of this work pave the way for designing high-

performance composite ceramic-polymer membranes with improved ionic conductivity, mechanical flexibility, and selectivity for next-generation NAqRFBs.

Author Contributions

Yasser Ashraf Gandomi: Conceptualization, Methodology, Software, Validation, Formal analysis, Investigation, Data curation, Visualization, Writing – original draft, Writing – review and editing. **Irina V. Krasnikova:** Conceptualization, Methodology, Software, Validation, Formal analysis, Investigation, Data curation, Visualization, Writing – original draft, Writing – review and editing. **Nikita Akhmetov:** Formal analysis, Investigation, Project administration, Data curation, Visualization, Writing – original draft, Writing – review and editing. **Nikolay Ovsyannikov:** Formal analysis, Investigation, Writing – original draft, Writing – review and editing. **Mariam A. Pogosova:** Formal analysis, Investigation, Project administration, Validation, Writing – original draft, Writing – review and editing. **Nicholas J. Matteucci:** Writing – original draft, Writing – review and editing. **Christopher T. Mallia:** Writing – original draft, Writing – review and editing. **Bertrand J. Neyhouse:** Visualization, Writing – original draft, Writing – review and editing. **Alexis M. Fenton Jr.:** Visualization, Writing – original draft, Writing – review and editing. **Fikile R. Brushett:** Conceptualization, Funding acquisition, Project administration, Resources, Supervision, Writing – original draft, Writing – review and editing. **Keith J. Stevenson:** Conceptualization, Funding acquisition, Project administration, Resources, Supervision, Writing – review and editing.

Corresponding Authors

Fikile R. Brushett (*brushett@mit.edu*), and Keith J. Stevenson (*k.stevenson@skoltech.ru*).

Acknowledgements

This work was funded by the Skoltech – MIT Next Generation Program. YAG, BJN, and FRB gratefully acknowledge support by the Joint Center for Energy Storage Research, an Energy Innovation Hub funded by the U.S. Department of Energy, Office of Science, Basic Energy Sciences. BJN and NJM gratefully acknowledge the NSF Graduate Research Fellowship Program under Grant Number 1122374. Any opinion, findings, and conclusions or recommendations expressed in this material are those of the authors and do not necessarily reflect the views of the NSF. CTM gratefully acknowledges support under and awarded by the Department of Defense, Office of Naval Research, through the National Defense Science and Engineering Graduate (NDSEG) Fellowship. The authors also thank Katharine Greco, Kara Rodby, and Kevin Tenny of the Brushett Research Group for fruitful discussions.

References

- (1) Milshtein, J. D.; Barton, J. L.; Carney, T. J.; Kowalski, J. A.; Darling, R. M.; Brushett, F. R. Towards low resistance nonaqueous redox flow batteries. *Journal of The Electrochemical Society* **2017**, *164* (12), A2487.
- (2) Kowalski, J. A.; Su, L.; Milshtein, J. D.; Brushett, F. R. Recent advances in molecular engineering of redox active organic molecules for nonaqueous flow batteries. *Current Opinion in Chemical Engineering* **2016**, *13*, 45-52.
- (3) Weber, A. Z.; Mench, M. M.; Meyers, J. P.; Ross, P. N.; Gostick, J. T.; Liu, Q. Redox flow batteries: a review. *Journal of applied electrochemistry* **2011**, *41* (10), 1137-1164.
- (4) Attanayake, N. H.; Kowalski, J. A.; Greco, K. V.; Casselman, M. D.; Milshtein, J. D.; Chapman, S. J.; Parkin, S. R.; Brushett, F. R.; Odom, S. A. Tailoring Two-Electron-Donating Phenothiazines To Enable High-Concentration Redox Electrolytes for Use in Nonaqueous Redox Flow Batteries. *Chemistry of Materials* **2019**, *31* (12), 4353-4363.
- (5) Milshtein, J. D.; Fisher, S. L.; Breault, T. M.; Thompson, L. T.; Brushett, F. R. Feasibility of a Supporting-Salt-Free Nonaqueous Redox Flow Battery Utilizing Ionic Active Materials. **2017**.
- (6) Darling, R. M.; Gallagher, K. G.; Kowalski, J. A.; Ha, S.; Brushett, F. R. Pathways to low-cost electrochemical energy storage: a comparison of aqueous and nonaqueous flow batteries. *Energy & Environmental Science* **2014**, *7* (11), 3459-3477.
- (7) Rodby, K. E.; Carney, T. J.; Ashraf Gandomi, Y. ; Barton, J. L.; Darling, R. M.; Brushett, F. R. Assessing the levelized cost of vanadium redox flow batteries with capacity fade and rebalancing. *Journal of Power Sources* **2020**, 227958.

- (8) Yuan, J.; Pan, Z.-Z.; Jin, Y.; Qiu, Q.; Zhang, C.; Zhao, Y.; Li, Y. Membranes in non-aqueous redox flow battery: A review. *Journal of Power Sources* **2021**, *500*, 229983.
- (9) Wu, J.; Dai, Q.; Zhang, H.; Li, X. Recent Development in Composite Membranes for Flow Batteries. *ChemSusChem* **2020**.
- (10) Gubler, L. Membranes and Separators for Redox Flow Batteries. *Current Opinion in Electrochemistry* **2019**.
- (11) Prifti, H.; Parasuraman, A.; Winardi, S.; Lim, T. M.; Skyllas-Kazacos, M. Membranes for redox flow battery applications. *Membranes* **2012**, *2* (2), 275-306.
- (12) Gvozdik, N. A.; Sanginov, E. A.; Abunaeva, L. Z.; Konev, D. V.; Usenko, A. A.; Novikova, K. S.; Stevenson, K. J.; Dobrovolsky, Y. A. A Composite Membrane Based on Sulfonated Polystyrene Implanted in a Stretched PTFE Film for Vanadium Flow Batteries. *ChemPlusChem* **2020**, *85* (12), 2580-2585.
- (13) Zeng, L.; Zhao, T.; Wei, L.; Jiang, H.; Wu, M. Anion exchange membranes for aqueous acid-based redox flow batteries: Current status and challenges. *Applied energy* **2019**, *233*, 622-643.
- (14) Merle, G.; Wessling, M.; Nijmeijer, K. Anion exchange membranes for alkaline fuel cells: A review. *Journal of Membrane Science* **2011**, *377* (1-2), 1-35.
- (15) Armstrong, C. G.; Hogue, R. W.; Toghiani, K. E. Characterisation of the ferrocene/ferrocenium ion redox couple as a model chemistry for non-aqueous redox flow battery research. *Journal of Electroanalytical Chemistry* **2020**, *872*, 114241.

- (16) Laramie, S. M.; Milshtein, J. D.; Breault, T. M.; Brushett, F. R.; Thompson, L. T. Performance and cost characteristics of multi-electron transfer, common ion exchange non-aqueous redox flow batteries. *Journal of Power Sources* **2016**, *327*, 681-692.
- (17) Montoto, E. C.; Nagarjuna, G.; Moore, J. S.; Rodríguez-López, J. Redox active polymers for non-aqueous redox flow batteries: validation of the size-exclusion approach. *Journal of The Electrochemical Society* **2017**, *164* (7), A1688-A1694.
- (18) Su, L.; Ferrandon, M.; Kowalski, J. A.; Vaughey, J. T.; Brushett, F. R. Electrolyte development for non-aqueous redox flow batteries using a high-throughput screening platform. *Journal of The Electrochemical Society* **2014**, *161* (12), A1905-A1914.
- (19) Senthilkumar, S.; Han, J.; Park, J.; Hwang, S. M.; Jeon, D.; Kim, Y. Energy efficient Na-aqueous-catholyte redox flow battery. *Energy Storage Materials* **2018**, *12*, 324-330.
- (20) Allcorn, E.; Nagasubramanian, G.; Pratt III, H. D.; Spoerke, E.; Ingersoll, D. Elimination of active species crossover in a room temperature, neutral pH, aqueous flow battery using a ceramic NaSICON membrane. *Journal of Power Sources* **2018**, *378*, 353-361.
- (21) Raja, M.; Angulakshmi, N.; Thomas, S.; Kumar, T. P.; Stephan, A. M. Thin, flexible and thermally stable ceramic membranes as separator for lithium-ion batteries. *Journal of membrane science* **2014**, *471*, 103-109.
- (22) Liang, X.; Han, D.; Wang, Y.; Lan, L.; Mao, J. Preparation and performance study of a PVDF-LATP ceramic composite polymer electrolyte membrane for solid-state batteries. *RSC advances* **2018**, *8* (71), 40498-40504.

- (23) Shi, X.; Ma, N.; Wu, Y.; Lu, Y.; Xiao, Q.; Li, Z.; Lei, G. Fabrication and electrochemical properties of LATP/PVDF composite electrolytes for rechargeable lithium-ion battery. *Solid State Ionics* **2018**, *325*, 112-119.
- (24) Tu, Z.; Kambe, Y.; Lu, Y.; Archer, L. A. Nanoporous polymer-ceramic composite electrolytes for lithium metal batteries. *Advanced Energy Materials* **2014**, *4* (2), 1300654.
- (25) Pogosova, M. A.; Krasnikova, I. V.; Sanin, A. O.; Lipovskikh, S. A.; Eliseev, A. A.; Sergeev, A. V.; Stevenson, K. J. Complex Investigation of Water Impact on Li-Ion Conductivity of Li_{1.3}Al_{0.3}Ti_{1.7}(PO₄)₃—Electrochemical, Chemical, Structural, and Morphological Aspects. *Chemistry of Materials* **2020**, *32* (9), 3723-3732.
- (26) Krasnikova, I. V.; Pogosova, M. A.; Sanin, A. O.; Stevenson, K. J. Toward Standardization of Electrochemical Impedance Spectroscopy Studies of Li-Ion Conductive Ceramics. *Chemistry of Materials* **2020**, *32* (6), 2232-2241.
- (27) Brown, E. N.; Dattelbaum, D. M. The role of crystalline phase on fracture and microstructure evolution of polytetrafluoroethylene (PTFE). *Polymer* **2005**, *46* (9), 3056-3068.
- (28) Ashraf Gandomi, Y.; Aaron, D. S.; Mench, M. M. Influence of membrane equivalent weight and reinforcement on ionic species crossover in all-vanadium redox flow batteries. *Membranes* **2017**, *7* (2), 29.
- (29) Forner-Cuenca, A.; Penn, E. E.; Oliveira, A. M.; Brushett, F. R. Exploring the role of electrode microstructure on the performance of non-aqueous redox flow batteries. *Journal of The Electrochemical Society* **2019**, *166* (10), A2230-A2241.

(30) Ashraf Gandomi, Y.; Aaron, D.; Houser, J.; Daugherty, M.; Clement, J.; Pezeshki, A.; Ertugrul, T.; Moseley, D.; Mench, M. Critical Review—Experimental Diagnostics and Material Characterization Techniques Used on Redox Flow Batteries. *Journal of The Electrochemical Society* **2018**, *165* (5), A970-A1010.

(31) Pogosova, M.; Krasnikova, I.; Sergeev, A.; Zhugayevych, A.; Stevenson, K. Correlating structure and transport properties in pristine and environmentally-aged superionic conductors based on $\text{Li}_{1-x}\text{Al}_x\text{Ti}_{1-x}\text{PO}_4$ ceramics. *Journal of Power Sources* **2020**, *448*, 227367.

(32) Ferreira, J.; Monteiro, T.; Lopes, A.; Costa, C.; Silva, M. M.; Machado, A.; Lanceros-Mendez, S. Variation of the physicochemical and morphological characteristics of solvent casted poly (vinylidene fluoride) along its binary phase diagram with dimethylformamide. *Journal of Non-Crystalline Solids* **2015**, *412*, 16-23.

(33) Jacob, M.; Prabakaran, S.; Radhakrishna, S. Effect of PEO addition on the electrolytic and thermal properties of PVDF- LiClO_4 polymer electrolytes. *Solid State Ionics* **1997**, *104* (3-4), 267-276.

(34) Shen, Y.; Reddy, M. J.; Chu, P. P. Porous PVDF with LiClO_4 complex as ‘solid’ and ‘wet’ polymer electrolyte. *Solid State Ionics* **2004**, *175* (1-4), 747-750.

(35) Pareek, T.; Dwivedi, S.; Ahmad, S. A.; Badole, M.; Kumar, S. Effect of NASICON-type $\text{LiSnZr}(\text{PO}_4)_3$ ceramic filler on the ionic conductivity and electrochemical behavior of PVDF based composite electrolyte. *Journal of Alloys and Compounds* **2020**, *824*, 153991.

(36) Huang, Q.; Choi, D.; Cosimbescu, L.; Lemmon, J. P. Multi-electron redox reaction of an organic radical cathode induced by a mesopore carbon network with nitroxide polymers. *Physical Chemistry Chemical Physics* **2013**, *15* (48), 20921-20928.

(37) Nakahara, K.; Iwasa, S.; Satoh, M.; Morioka, Y.; Iriyama, J.; Suguro, M.; Hasegawa, E. Rechargeable batteries with organic radical cathodes. *Chemical Physics Letters* **2002**, *359* (5-6), 351-354.

(38) Wei, X.; Xu, W.; Vijayakumar, M.; Cosimbescu, L.; Liu, T.; Sprenkle, V.; Wang, W. TEMPO-based catholyte for high-energy density nonaqueous redox flow batteries. *Advanced Materials* **2014**, *26* (45), 7649-7653.

(39) Small, L. J.; Pratt III, H. D.; Fujimoto, C. H.; Anderson, T. M. Diels Alder polyphenylene anion exchange membrane for nonaqueous redox flow batteries. *Journal of The Electrochemical Society* **2015**, *163* (1), A5106.

(40) Ashraf Gandomi, Y.; Aaron, D.; Mench, M. Coupled membrane transport parameters for ionic species in all-vanadium redox flow batteries. *Electrochimica Acta* **2016**, *218*, 174-190.